GEOPHYSICS, VOL. 82, NO. 6 (NOVEMBER-DECEMBER 2017); P. P119–P128, 12 FIGS., 4 TABLES.
10.1190/GEO2016-0674.1

Low-frequency acoustic signal created by rising air-gun bubble

Daniel Wehner[1] and Martin Landrø[1]

ABSTRACT

In the seismic industry, there is increasing interest in generating and recording low frequencies, which leads to better data quality and can be important for full-waveform inversion. The air gun is a seismic source with a signal that consists of the (1) main impulse, (2) oscillating bubble, and (3) rising of this air bubble. However, there has been little investigation of the third characteristic. We have studied a low-frequency signal that could be created by the rising air bubble and find the contribution to the low-frequency content in seismic acquisition. We use a simple theory and modeling of rising spheres in water and compute the acoustic signal created by this effect. We conduct tank and field experiments with a submerged buoy that is released from different depths and record the acoustic signal with hydrophones along the rising path. The experiments simulate the signal from the rising bubble separated from the other two effects (1 and 2). Furthermore, we use data recorded below a single air gun fired at different depths to investigate if we can observe the proposed signal. We find that the rising bubble creates a low-frequency signal. Compared with the main impulse and the oscillating bubble effect of an air-gun signal, the contribution of the rising bubble is weak, on the order of 1/900 depending on the bubble size. By using large air-gun arrays tuned to create one big bubble, the contribution of the signal can be increased. The enhanced signal can be important for deep targets or basin exploration because the low-frequency signal is less attenuated.

INTRODUCTION

The interest in enhancing the low-frequency content in seismic data has increased within the last years because there are three main benefits due to broadband seismic data: (1) Low frequencies reduce the side lobes of wavelets leading to higher resolution, (2) they penetrate deeper into the earth because they suffer less from attenuation, and (3) low-frequency data are important for seismic inversion (ten Kroode et al., 2013). A general overview of recent advances in broadband seismology is given by Robertsson et al. (2013), who divide the topic in benefits of low-frequency data, new methods in processing, imaging processes, and advances in acquisition of low-frequency data. This study focuses on acquisition and more precisely on a source mechanism of seismic air guns that potentially could create low frequencies.

In marine seismic acquisition, the data recording has improved due to two main approaches. On the one hand, data are recorded with variable-depth streamers. Dhelie et al. (2014) show data from a snake streamer acquisition, where the receivers are located at different depths, whereas Soubaras and Lafet (2013) explain processing techniques for variable streamer depth acquisition. Additionally, Hicks et al. (2014) demonstrate that advanced processing of flat streamer data could reveal results similar to advanced processing of a variable depth streamer. On the other hand, multicomponent receivers are used to measure pressure and particle velocity (Carlson et al., 2007) at the same depth. Using proper processing techniques, both methods reduce the notches in the frequency spectrum that are related to the ghost reflections from the surface (Ikelle and Amundsen, 2005). The improved data quality is achieved by separation of the upgoing and downgoing wavefield. Furthermore, Landrø et al. (2014) suggest using geophones instead of hydrophones at the ocean bottom to record more signal in the low-frequency band.

On the source side, Moldoveanu (2000) suggests firing air guns on a vertical source array configuration where two air-gun arrays are located at different depths. These arrays can be fired simultaneously or with a little time delay between individual air guns (Abma and Ross, 2013). Firing source arrays at different depths with a time delay to create a constructive downgoing wavefield is beneficial for low frequencies (Cambois et al., 2009). Shooting the air guns at variable depths is another approach to improve the frequency content of the signal (Haavik and Landrø, 2015). These methods are still under investigation, and the more complicated the shooting pattern, the more demanding is the processing of the data. If the

Manuscript received by the Editor 12 December 2016; revised manuscript received 27 June 2017; published ahead of production 30 August 2017; published online 23 October 2017.
[1]Norwegian University of Science and Technology, Department of Geoscience and Petroleum, Trondheim, Norway. E-mail: daniel.wehner@ntnu.no.

processing can be handled, the sequential shooting at various depths seems promising for an increased low-frequency signal.

As the previous developments are related to array design, there are also improvements on single sources. Coste et al. (2014) present a new design of air guns that reduces amplitudes at high frequencies to mitigate the effect on marine mammals. In addition, major research efforts are carried out on marine vibrators. On land, seismic vibrators can produce reproducible low-frequency signals very efficiently (Wei et al., 2012). In the marine area, this is still challenging. However, Pramik et al. (2015) and Ozasa et al. (2015) show promising results for this technique. Furthermore, Meier et al. (2015) illustrate a marine dipole source that would especially increase the energy content at the low-frequency end of the spectrum. Recently, an "FWI-friendly" vibrator-type source that focuses on creating ultralow frequencies is presented by Dellinger et al. (2016).

In this paper, we explore a mechanism from seismic air guns that could be partly responsible for the creation of low frequencies. Landrø and Amundsen (2014a) discuss the impact of source depth on the low-frequency output, where they find enhanced low frequencies (less than 1 Hz) for shallow source depths at 3.00 m compared with 7.50 m. Based on this result, they suggest that these low frequencies could be created by the rising of the air-gun bubble in the water column (Landrø and Amundsen, 2014b). We present a simple theory and modeling that explains the signal from a rising sphere that is extensively studied in fluid dynamics. Furthermore, we compare the theoretical results with data recorded during tank and field experiments where a submerged buoy is released from different water depths. The experiment should separate the signal created by the rising bubble from the main impulse and oscillating behavior of the air-gun bubble, which are much stronger in amplitude. Additionally, we check the model against single air-gun recordings from different depths to demonstrate that the acoustic signal of a rising air bubble can be measured. Finally, we investigate the exploitation of the signal for real applications in seismic exploration and crustal studies. The results should prove the existence of the signal from a rising air-gun bubble and hence reinforce the mechanism proposed by Landrø and Amundsen (2014b).

THEORY

We are interested in the acoustic signal created by a rising air bubble only. Therefore, the movement of a sphere through a fluid and the corresponding pressure distribution around the sphere are described.

If a sphere is submerged in water, gravity, buoyancy, and drag are the forces acting on the object. The problem is well-described in fluid dynamics where it is seen similar to the flow around a fixed sphere (Morrison, 2013). The force balance, assuming that the movement is in the z-direction only, is given as (Morrison, 2013)

$$F_B - F_G - F_D = ma_z, \tag{1}$$

with

$$F_B = V\rho_f g, \tag{2}$$

$$F_D = \frac{1}{2}\rho_f C_D A v_z^2, \tag{3}$$

$$F_G = V\rho_s g, \tag{4}$$

where F_B is the buoyancy, F_D is the drag, and F_G is the gravitational force. The volume and cross-sectional area of the sphere are denoted by $V = (4/3)\pi R^3$ and $A = \pi R^2$ with radius R, whereas ρ_s is its density and m is the mass. The density of the fluid is ρ_f, g is the gravitational acceleration, and C_D is the drag coefficient that depends on the fluid type. The vertical velocity and acceleration are denoted by v_z and a_z, respectively. Equation 1 can be reorganized to solve for the acceleration

$$a_z = \frac{F_B - F_G - F_D}{m}. \tag{5}$$

Integration of equation 5 gives us the velocity, and further integration gives the position of the sphere (Halliday et al., 2003):

$$v_z = \int a_z dt, \tag{6}$$

$$z = \int v_z dt. \tag{7}$$

The velocity v_z is an important quantity for the source term of the acoustic signal, as we will see later. The buoyancy and gravitational force are constant assuming that the size and density of the sphere are not changing, and g is constant. However, the drag force depends on v_z and C_D (equation 3) that change over time. The drag coefficient C_D is dependent on the Reynolds number that discriminates between laminar and turbulent flow and is given as (Morrison, 2013)

$$\mathrm{Re} = \frac{v_z D}{\nu}, \tag{8}$$

where D is the diameter of the sphere and ν is the kinematic viscosity of the fluid. The empirical relation between the drag coefficient and the Reynolds number is shown in Figure 1 (Morrison, 2013). So far, we are able to describe the movement of a rising sphere assuming a perfect spherical shape with a constant size and density.

The pressure distribution surrounding the sphere created from this movement depends on whether the flow regime is laminar or turbulent. For laminar flow, the pressure distribution C_P is given as (Michelson, 1970)

$$C_P = 2\frac{R^3}{r^3} - 3\frac{R^3}{r^3}\sin^2(\theta) - \frac{R^6}{r^6}\cos^2(\theta) - \frac{R^6}{4r^6}\sin^2(\theta), \tag{9}$$

where r is the distance to the observation point and θ is the angle surrounding the sphere. Figure 2a shows the pressure around a sphere for laminar flow, where the amplitude is normalized to the maximum value. For Reynolds numbers higher than Re = 2100, turbulent flow is expected (Reynolds, 1883). Achenbach (1972) already performed flow experiments around a fixed sphere within a turbulent flow regime where the pressure behind the sphere changes with respect to laminar flow. Figure 2c shows results for different Reynolds numbers where we have negative pressure behind the sphere instead of positive pressure as in the laminar case. We modify equation 9 according to the experimental results from Achenbach (1972). The pressure distribution from 0° to 110° is assumed to be the same as for the laminar case, whereas the pressure distribution from 110° to 180° is set to a

fixed value taken from the angle at 110°. This leads to a negative pressure behind the sphere (Figure 2b) fitting the experimental data from Achenbach (1972).

The source strength, which gives the acoustic energy density emitted by the rising sphere, is controlled by its velocity v_z (equation 6). A terminal, constant velocity will be achieved when the forces (equation 1) are in balance, which defines the upper limit for the source strength. The source term can be written as (Morrison, 2013)

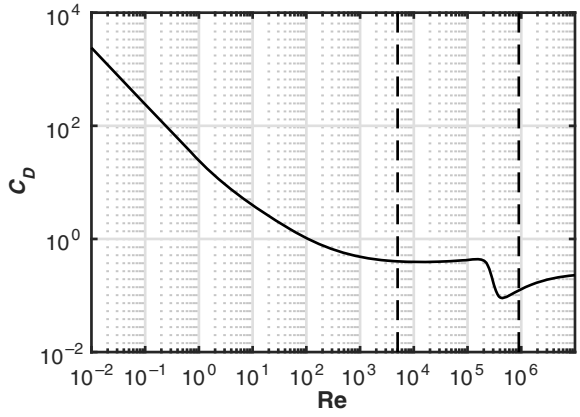

Figure 1. Empirical relation between the drag coefficient and the Reynolds number from experimental data (Morrison, 2013). The area between the dashed lines indicates the expected Reynolds numbers for our experiments.

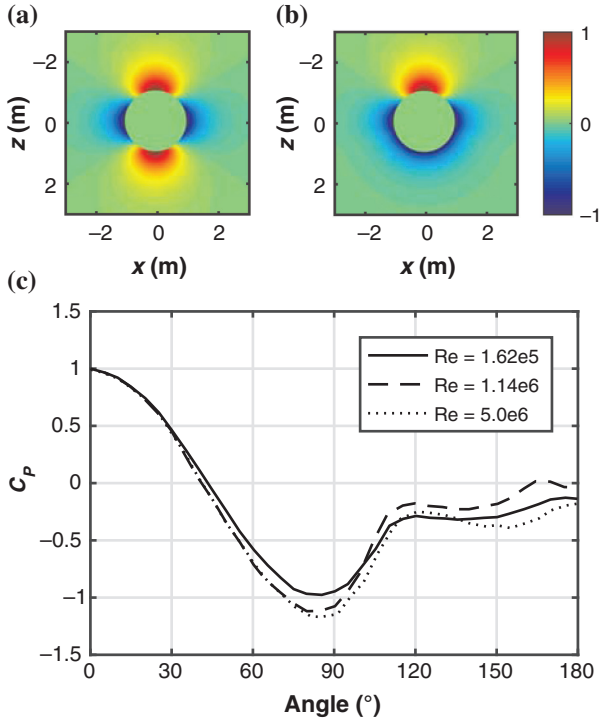

Figure 2. (a) Pressure distribution around a sphere at laminar flow (Michelson, 1970), (b) modified pressure distribution for turbulent flow according to the results of Achenbach (1972). The flow direction is vertical, pointing in the negative z-direction, and (c) experimental data from (Achenbach, 1972) for a turbulent flow around a fixed sphere. All amplitudes are normalized to the maximum positive pressure value.

$$S = \frac{\rho_f v_z^2}{2}. \tag{10}$$

The modified equation 9 combined with equation 10 is the pressure field emitted from the rising sphere in the near-field with an amplitude decay of R^3/r^3 (equation 9). Hence, the near-field pressure is given as

$$p_{\text{near}} = SC_P. \tag{11}$$

We estimate the transition between the near- and far-field r_{far} at three times the source size, which is described by the radius R. In the far field, the amplitude decay is R/r according to Gilmore (1952) and the emitted pressure can be written as

$$p_{\text{far}} = SC_P(r_{\text{far}})\frac{R}{r}. \tag{12}$$

Here, we assume that the movement of a rising sphere is similar to the movement of the wall of an oscillating bubble, as described by Gilmore (1952). This assumption is valid for the movement vertically below the sphere. For radiating angles deviating from the vertical line, this assumption is less exact because the movement from the sphere is only upward and not toward the center such as during an oscillation of a sphere. Furthermore, the pressure calculations hold for the case of an incompressible fluid. This could be assumed because the rising velocity of the sphere is much smaller than the velocity of acoustic sound in water (Gilmore, 1952). However, this is a simple theory describing the acoustic pressure emitted by a rising sphere, which we think is comparable with the rising of an air-gun bubble.

MODELING

The movement and acoustic pressure from the rising sphere are modeled according to the theory. The problem is solved with a finite-difference approach using a two-stage explicit Runge-Kutta method (LeVeque, 2007)

$$U^{\text{mid}} = U^n + \frac{1}{2}f(U^n)\Delta t, \tag{13}$$

$$U^{n+1} = U^n + f(U^{\text{mid}}), \tag{14}$$

where U denotes the depth z, velocity v_z, or acceleration a_z of the sphere, and Δt is the time step, where the time $t = n\Delta t$ ($n = 1, 2, \ldots$). The initial depth z^0 is known, and we assume an initial velocity v_z^0 close to zero, which we can use to compute the initial acceleration a_z^0. First, the quantities v_z and z are computed between two adjacent time steps with the Euler method according to equation 13:

$$v^{\text{mid}} = v^n + \frac{1}{2}a^n\Delta t, \tag{15}$$

$$z^{\text{mid}} = z^n + \frac{1}{2}v^n\Delta t. \tag{16}$$

In a second step, the drag coefficient, using the Reynolds number (equation 8) and empirical relations (Figure 1), and the drag force (equation 3) can be computed for the midpoint. Hence, we can calculate the acceleration a^{mid} (equation 5) at the same position. We can use these values to compute our quantities for the next time step

$$v^{n+1} = v^n + a^{\text{mid}}\Delta t, \tag{17}$$

$$z^{n+1} = z^n + v^{\text{mid}}\Delta t. \tag{18}$$

Now, we can compute the drag coefficient, drag force, and acceleration a^{n+1} for the new time step and repeat the scheme. Because we have the description of the moving sphere (z, v_z, a_z) at all times, we can use the velocity to model the pressure field surrounding it using equations 11 and 12.

The two-stage explicit Runge-Kutta method has second-order accuracy (LeVeque, 2007). But keep in mind that we make several assumptions to simplify the problem as stated at the end of the "Theory" section.

EXPERIMENTS

We perform experiments in a water tank and in the open sea where submerged buoys of different sizes are released from several depths. We denote the three different buoy sizes by buoys *A*, *B*, and *C*. Due to practical reasons, buoy *A* and *B* are used in the tank, whereas buoys *B* and *C* are used in the field experiment. The important parameters of all buoys are listed in Table 1.

In both experiments, Bruel and Kjær hydrophones type 8105 are used, which have a frequency range between 0.1 Hz and 180 kHz. Additionally, the rising buoy is recorded on video in the tank and field experiment to measure the depth at different time steps and hence the velocity of the buoy.

Furthermore, we use data from an air-gun experiment, in which a single gun was fired at different depths in the open sea (Landrø and Amundsen, 2014b).

Buoy experiment in the tank

Figure 3 shows the setup for the tank experiment. The depth and width of the tank are indicated in the figure, and the length is 6 m, approximately 3 m to each side of the buoy. A weight at the bottom and a rope are used to submerge and release the buoy from four different depths denoted by z_s. A four-hydrophone array is placed along the rising path of the buoy, where the first one (H1) is closest to the water surface. A video camera, located at half the depth z_s, records the rising sphere with 30 fps, which means that a photo is taken every 33 ms.

Table 1. Essential parameters of the three buoys used for the experiments.

Buoy dimensions			
Buoy name	*A*	*B*	*C*
Radius R (m)	0.10	0.12	0.145
Mass m (kg)	0.7	1.1	2.0
Effective density ρ_b (kg/m^3)	167	152	157

The major advantage of the tank experiment is the high accuracy that can be achieved for the release depth z_s, the depth of the hydrophones, and the offset between the source and receiver. However, some issues occur during the experiment, which should be mentioned. The rising buoy creates small gravity waves while it gets close to the surface that could interfere with the signal of interest. Due to the limited size, side and surface reflections are expected. We think these are negligible because we conduct the test in the middle of the tank and measure the signal very close to the source. Although we have high precision of the receiver and source geometry, the buoy is not a perfect sphere and turbulences are created while the buoy rises. Therefore, the buoy is not rising along a straight vertical line, which could lead to errors in offset and hence in the amplitude estimation.

Buoy experiment in the field

The field experiment is conducted in a fjord in Norway, and the setup is similar to the tank experiment (Figure 4). During this test, only two hydrophones are available. The release depths z_s and the offset x are larger compared with the tank experiment. For practical reasons, buoys *B* and *C* are used for these tests. The rising buoy was again recorded by a video camera located approximately at half the release depth.

The test was carried out to reproduce the signal from the tank experiment without a limiting medium in the x- and y-directions. One major disadvantage of this test is less accuracy in the position of the buoy and hydrophones because the visibility within the water was less than 4 m and the experiment was influenced by tidal effects. This led to errors for the release depth within ±0.8 m. As already mentioned, the buoy is not rising along a straight vertical line. This effect is more pronounced if the release depth is increased. Additionally, the background noise is higher than in the tank experiment, which was also increased by a fishing farm a few hundred meters away.

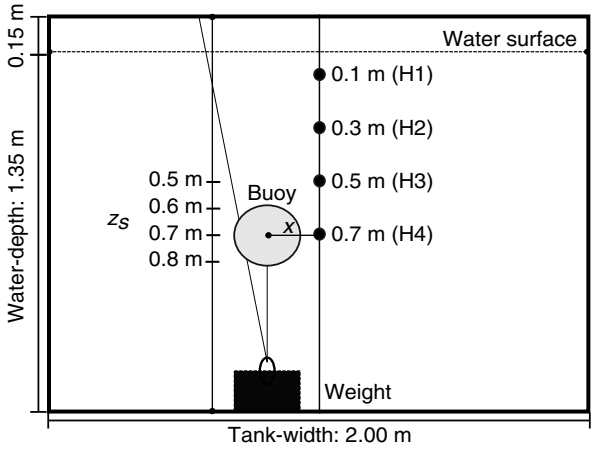

Figure 3. Cross section of the setup for buoy experiments in the tank. The depth and width of the tank are indicated, and the length is 3 m to each side of the buoy. H1, H2, H3, and H4 denote the hydrophones, z_s is the release depth of the buoy, and x is the offset between source and receiver.

Air-gun experiment in the field

We use air gun data recorded during a field test in a Norwegian fjord some years ago (Landrø and Amundsen, 2014b). A single 600 in^3 air gun was fired at four different depths, which are 3, 5, 7.5, and 10 m, respectively (Figure 5). A hydrophone recorded the signal at a constant distance of 20 m below the air gun. The total water depth was 390 m, and the weather conditions were excellent, which led to a good repeatability of single shots at the same depth. That an air gun creates stable signatures is demonstrated by Dragoset et al. (1987). The signatures of the air gun fired at the same depth show similar characteristics for the signal under investigation.

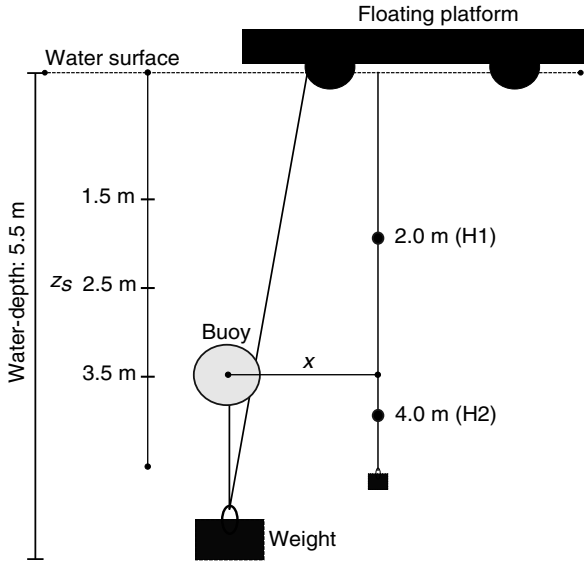

Figure 4. Cross section of the setup for buoy experiments in the field. H1 and H2 denote the hydrophones, z_s is the release depth of the buoy, and x is the offset between source and receiver.

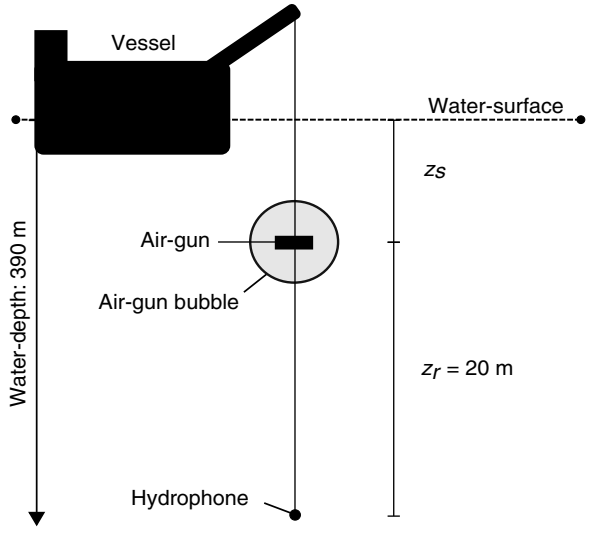

Figure 5. Cross section of the setup for air-gun experiments in the field. The gun is fired at four different depths z_s (3, 5, 7.5, 10 m), and the vertical offset z_r is constant.

RESULTS

The results of the buoy experiments in the tank, field, and the air-gun data will be compared with the model to demonstrate that the proposed negative acoustic signal is created by a rising bubble and that it is measurable. The amplitudes of the acoustic signal are given in bar units, and 1 bar $= 10^5$ Pa.

Buoy in the tank

First, we compare the video recorded data with the modeled movement of a sphere to show that the simple theory is a good approximation explaining the mechanism that is responsible for the signal we are looking for. In Figure 6, the modeled depth and velocity for the release of buoy B at $z_s = 0.75$ m is compared with depth measurements taken from the video.

The measured velocity is computed from the depth data. The maximum error between a measured and modeled depth is approximately 6 cm. This could be due to the simplified model, but it could also be due to errors in the depth measurement because only one photo is taken every 33 ms. We also recognize that the velocity reaches the terminal, constant velocity at 0.25 s, before it slows down. The decreasing velocity in the model is due to fewer buoyancy forces when the buoy is partly above the water surface. The good fit between the modeled and measured movement confirms that the main behavior of the buoy is described by the model.

We compare the measured acoustic signal from the rising buoy in the tank with the modeled signal using the proposed theory. It should be mentioned that the recorded data are not processed. Figure 7 illustrates the measured and modeled data for buoy A for two different release depths and an offset of $x = 0.15$ m. The time starts when the buoy is released, and the model stops when the center of the buoy has reached the surface, which is indicated by the vertical dotted line in the figure. We observe that the model has a good fit with the measured data showing the negative signal that we expect when the buoy passes the hydrophone. Also, the duration of the signal increases while the source depth increases (Figure 7b).

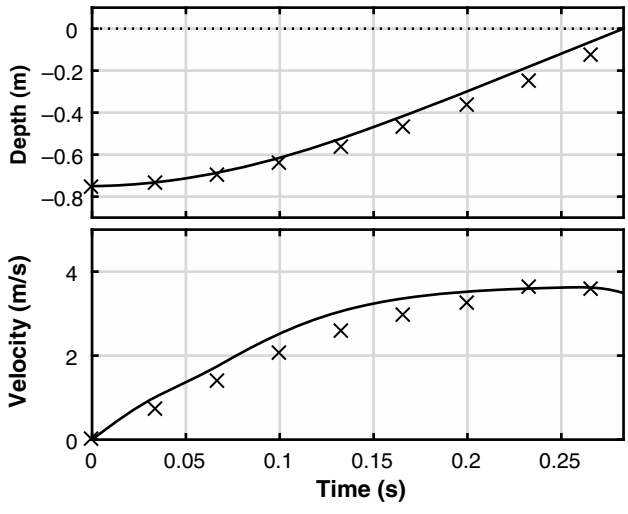

Figure 6. (a) Modeled (solid line) versus video-measured (crosses) depth position of buoy B in the tank during rising and (b) modeled (solid) versus video-measured (crosses) velocity of buoy B in the tank during rising.

The difference in amplitude between measured and modeled data could be due to the fact that the buoy is not rising along a straight vertical path, and hence the offset in the experiment is changing while it is constant in the model. That is confirmed because the difference in amplitudes is more pronounced for the deeper release depths where the rising path could deviate more from a straight vertical line. The amplitudes for the negative signal of H1 and H2 in Figure 7b are very similar, indicating that the buoy could have reached terminal velocity. This is not the case for the shallow release depth (Figure 7a) because the rising time is too short to reach the terminal velocity. The signal after the buoy has reached the surface, behind the dotted line, is probably related to gravity waves in the tank due to the buoy breaking the surface.

In Figure 8, we compare the measured and modeled data for the same release depths, but using buoy B and an offset of $x = 0.18$ m. The model fits the measured data well with some differences in the amplitude. These are probably also due to changing offsets while the buoy is rising. It should be noticed that the duration of the signal is shorter for buoy B than A because the buoyancy of the bigger buoy is higher and hence it rises faster.

The higher velocity v_z leads to higher amplitudes that could be observed if you compare Figures 7 and 8 carefully. The difference should be bigger if the same offset in both experiments is used.

Buoy in the field

We can verify the model once more by comparing it with the video recordings acquired during the field experiment. The modeled and measured depth and velocity are shown in Figure 9b. Additionally, a sequence of pictures illustrates the data used for measuring the depth (Figure 9a). The sequence starts at the upper left and finishes at the lower right panel while going from left to right. The time step between the pictures is 50 ms, whereas a picture every 8 ms exists for the plots of Figure 9b. We observe that the model predicts a faster rising than the measured data with a maximum error of 13 cm for a depth point. The deviation is higher than for the tank experiment, which could be due to the increased release depth. Therefore, the rising path deviates even more from a straight line, which leads to errors in the estimated rising time. Additionally, the release of the buoy was more complicated because of the deep water

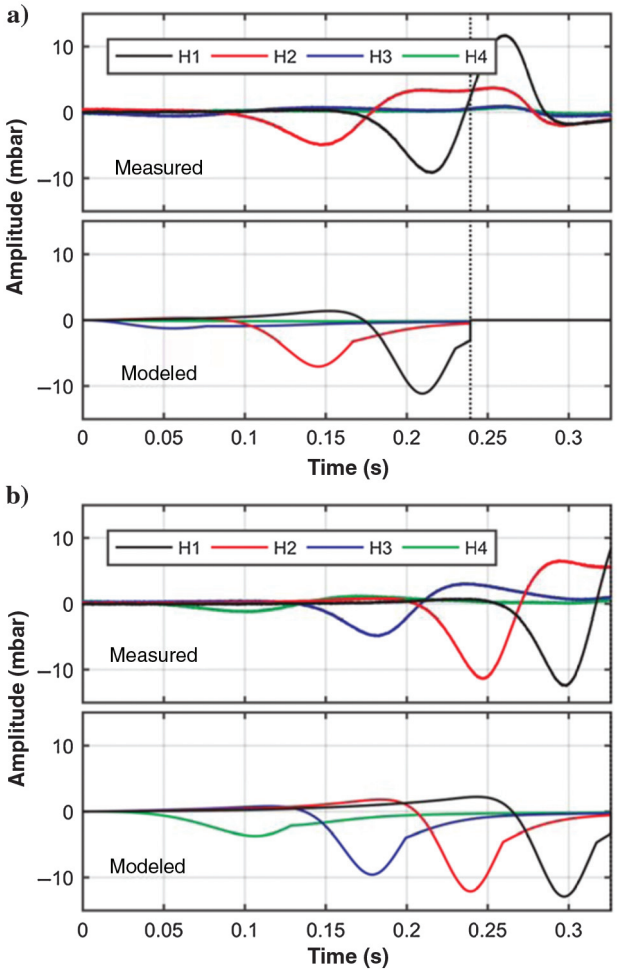

Figure 7. (a) Measured (top) and modeled signal (bottom) for the rising buoy A from a depth of $z_s = 0.50$ m, (b) measured (top) and modeled signal (bottom) for the rising buoy A from a depth of $z_s = 0.80$ m in the tank according to Figure 3. The vertical dotted line indicates the time when the center of the buoy is at the water surface.

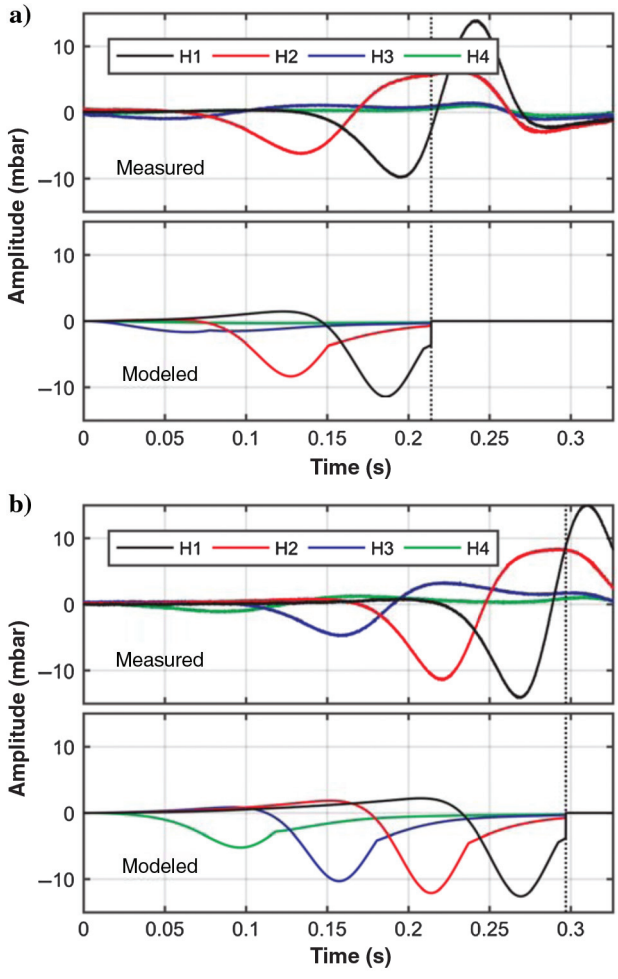

Figure 8. (a) Measured (top) and modeled signal (bottom) for the rising buoy B from a depth of $z_s = 0.50$ m. (b) Measured (top) and modeled signal (bottom) for the rising buoy B from a depth of $z_s = 0.80$ m in the tank according to Figure 3. The vertical dotted line indicates the time when the center of the buoy is at the water surface.

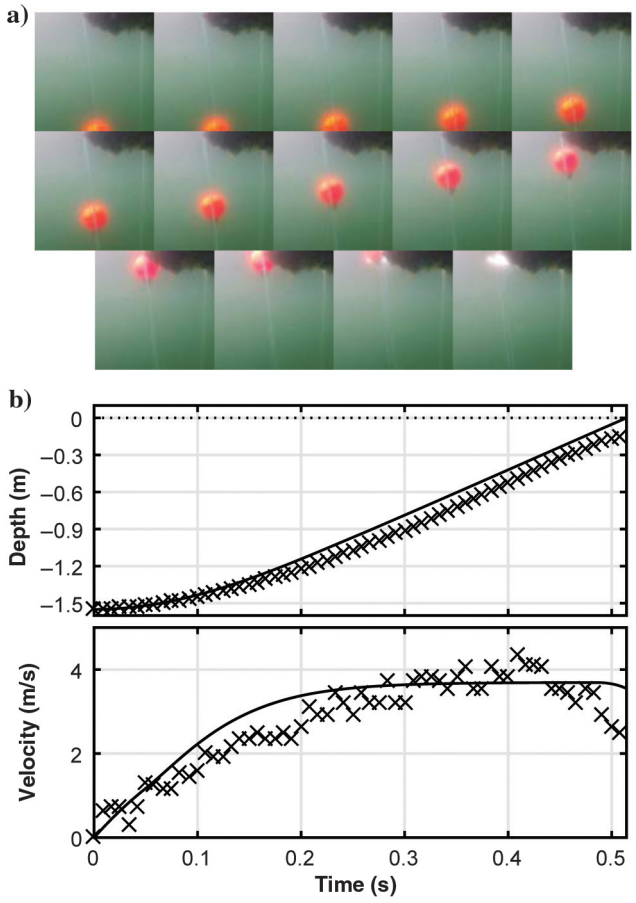

Figure 9. (a) Sequence of pictures from rising buoy with time step of 50 ms, (b) modeled (solid line) versus video measured (crosses) depth position of buoy *C* in the field during rising (top) and modeled (solid) versus video measured (crosses) velocity of buoy *C* in the field during rising (bottom).

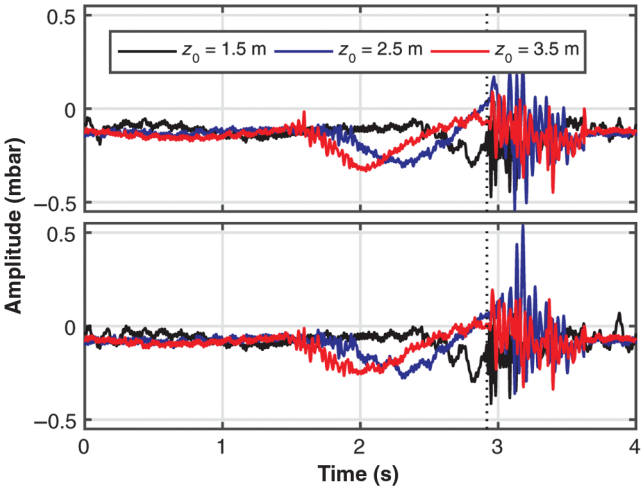

Figure 10. Recordings of (a) H1 and (b) H2 for release depths of 1.5, 2.5, and 3.5 m according to Figure 4. The signals are aligned to the buoy breaking the surface (at 2.9 s), indicated by the vertical dotted line.

depth and simple release mechanism, which could also create deviations between modeled and measured rising times.

Due to the high uncertainties in the release depth and the offset, it is difficult to adjust the model to these conditions. Therefore, we only use the measured data from different depths and both hydrophones (Figure 4) to demonstrate that the same signal is created in the open sea and for bigger offsets. The recorded signal for three release depths and an offset of $x = 1.25$ m for buoy *C* can be seen in Figure 10. The acoustic signal is 45 Hz low-pass filtered to remove background noise (e.g., electrical noise), and the signals are aligned to the high-amplitude, high-frequency signal at approximately 2.9 s (dashed line). This signal is related to the time when the buoy breaks the surface and hits the platform (Figure 4), which is therefore a good trigger at the end of the rising path.

We notice the higher noise level within the first second of the recording, but we also notice that a negative pressure signal starts approximately 1.5 s for the deepest release (red curve) and later for the shallower releases. Because the hydrophones are deeper than the buoy for most of the time during the rising, this demonstrates the negative pressure below the buoy. Also, the duration of the signal increases with increasing depth. The amplitudes at each hydrophone are similar for all depths, which is reasonable if we assume that the terminal velocity is achieved 0.25 s after the release (Figure 9b). Furthermore, we observe higher amplitudes for H1, which is explained by the shorter offset to the buoy while it rises. Also, it should be mentioned that the negative signal has more high-frequency noise than in the tank. This could be due to the higher background noise or to high turbulences as buoy *C* reaches higher velocities than *A* and *B* in the tank.

Air gun in the field

We need to estimate the size and density of the air-gun bubble to compare our model with the measured data. The Rayleigh equation is used to estimate the radius of the air-gun bubble, and then different percentages of the maximum radius are used for the modeling. This should be a simple approximation to account for the oscillating bubble because different radii have different rising velocities. For the biggest air bubble according to the shallowest firing depth, we use a radius of 75% of the maximum value, that is, 1 m. The radii of deeper firing depths are chosen the same way with percentages of 70%, 65%, and 60%, respectively. These differences should account for more and shorter oscillations that occur at deeper depths. Additionally, the bubble gets more dissolved during longer rising paths, and therefore further away from a spherical shape. The density of the air-gun bubble is assumed to be 230 kg/m^3, estimated from a fit to the modeled data. The deviation from the density of air is due to the oscillating effect where the air is expanded and compressed. Furthermore, the air-gun bubble is not a perfect sphere and can contain water particles that increase its density.

Figure 11a shows the recorded air-gun signal 20 m below the source, which is fired at four different depths. The main impulse occurs at time $t = 0$ s, and the amplitude scale is cut at 15 mbar to get greater focus on the signal afterward. We observe that the amplitude of the oscillating bubble increases and its period decreases with increasing water depth. In Figure 11b, the same signal is plotted, but it is magnified to a different time window and filtered with a 5 Hz low-pass filter. The difference in the amplitude scale between Figure 11a and 11b should be noticed. Additionally, the modeled signal of a rising sphere is displayed in Figure 11b (dotted lines).

The model stops when the center of the sphere is at the surface, and therefore it is shorter for shallow release depths.

On the one hand, we observe that the negative signal has the biggest amplitude for the shallowest firing depth; that could be related to the biggest bubble radius while the amplitude is decreasing for deeper source depths. On the other hand, the duration of the negative signal increases with increasing source depths. This is probably related to the longer rising path. Furthermore, the signal is smooth for the shallowest source depth, whereas it becomes more indistinct with increasing depth. This could be due to the fact that the air bubble gets more dissolved on its rising path, and this is more pronounced for longer rising times. In addition, the amplitude decreases gradually after its maximum negative value, which could be explained by the increasing distance between the rising bubble and the hydrophone. In general, the amplitude fit between the modeled and measured data is quite good, and also the increasing period fits to some extent. There are still several deviations between the modeled and measured data. These are probably due to the simplified model neglecting the oscillations of the bubble and compressible flow. However, the goal was to separate the signal of a rising bubble from the oscillating effect, and the main features of decreasing amplitude and increasing period with increasing source depth are explained by the model.

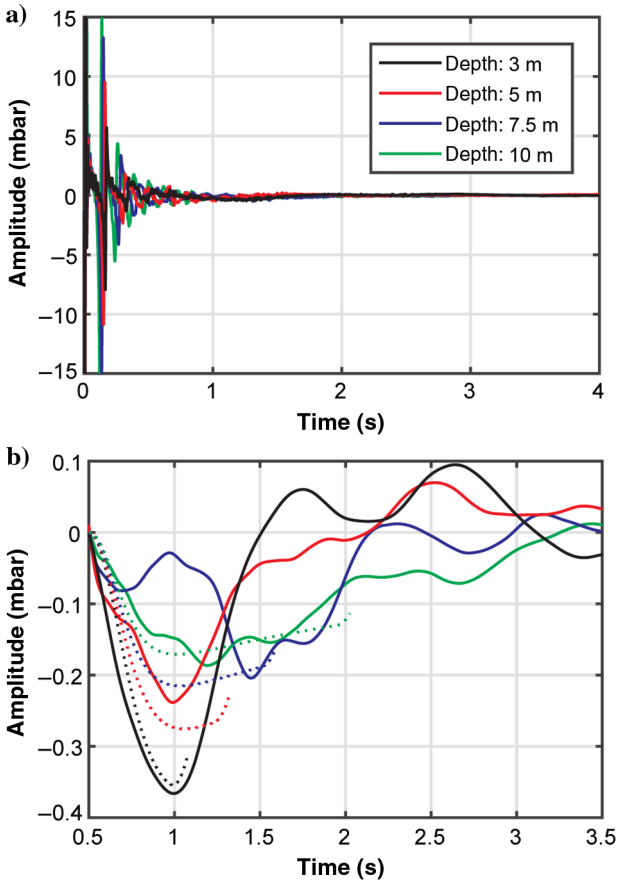

Figure 11. (a) Recorded air-gun signature, 150 Hz low-pass filtered, at hydrophone according to Figure 5, (b) zoom on recorded data between 0.5 and 3.5 s, 5 Hz low-pass filtered (solid line). Modeled signature of rising sphere (dashed line); the model stops when the sphere reaches the surface. Notice the different amplitude scale between (a and b).

DISCUSSION

We were able to measure a low-frequency acoustic signal created by a rising sphere by dedicated buoy experiments. The signal found in the air-gun data is likely to be the rising air bubble, which would confirm the far-field radiation of this acoustic signal. The simple theory and model are in good agreement with the experimental data and hence reinforce the proposed mechanism. However, the contribution of this effect compared with the main impulse and oscillating behavior from the air-gun bubble seems to be very small (Figure 11). For a source depth of $z_s = 7.5$ m, the near-field amplitude for the main impulse is 3.5 bar-m and for the rising bubble signal 0.0038 bar-m, whereas the main frequencies of both signals are 60 and 2 Hz, respectively. This leads to an amplitude ratio in the near-field of 1:900 for the single air-gun experiment, which would differ depending on the bubble size.

For a better comparison of both signal strengths, we illustrate a simple example of reflection seismic. The 3D model consists of a thin water layer, where the source and receiver are located at a depth of $z_s = 7.5$ m and $z_r = 30$ m, respectively. Below the water layer, the acoustic medium consists of a homogeneous sand layer with a thickness of $d = 3000$ m on top of a homogeneous half-space. The interface simulates the target area for our reflection example. We like to estimate the amplitudes of both signals recorded at the receiver after traveling through the medium because the impact of attenuation and source ghost depends on the frequency. The amplitudes at the receiver can be estimated as

$$A(f_i) = A_0(f_i) R G e^{\left(\frac{-\pi f_i z}{Q v_m}\right)} H(f_i), \tag{19}$$

where the medium velocity v_m and quality factor Q are assumed to be constant, z is the distance that the signal has traveled and $A_0(f_i)$ is the near-field amplitude. The main frequencies of the impulse and rising air-gun bubble are indicated by f_1 and f_2, respectively, with $i = 1, 2$. The reflection coefficient at the interface to the half-space and the geometric spreading are given as R and $G = 1/z$, whereas $H(f_i) = |2 \sin[(2\pi f_i z_s)/c]|$ is the source-ghost function with c as the sound velocity in water.

Results for amplitudes $A(f_i)$ for different combinations of medium velocities v_m and Q-values are listed in Table 2. For the computation, the reflection coefficient is assumed to be $R = 0.2$ according to a velocity and density change of 10% between both layers. We observe that the higher the attenuation (smaller Q) or slower the velocity, the smaller the amplitudes $A(f_i)$. Additionally, the advantage of low frequencies becomes obvious. The impact of different medium parameters on the low-frequency signal from the

Table 2. Amplitude of the main impulse $A(f_1)$ and the rising bubble signal $A(f_2)$ after traveling through a 3D medium with common medium parameters v_m, Q for a sandstone (Mavko et al., 1998).

v_m (m/s)	Q	$A(f_1)$ (bar)	$A(f_2)$ (bar)
3000	150	18.0e-6	0.014e-6
3000	300	63.2e-6	0.015e-6
4000	150	33.7e-6	0.015e-6
4000	300	86.5e-6	0.016e-6

rising bubble is less compared with the high-frequency signal, and hence the low-frequency signal is especially valuable for media with low v_m- and Q-values. However, the noise on streamer data in rough weather has amplitudes of approximately 46e-6 bar for frequencies less than 5 Hz and 6e-6 bar for higher frequencies (Landrø et al., 1989). During calm weather, the noise level could be reduced by a factor of 3 or 4, leading to optimal noise amplitudes approximately 11e-6 bar for the low and 1.5e-6 bar for the high frequencies. Although the signal of the main impulse is above the noise level, the signal of the rising bubble is too low to be recorded. Therefore, we need to find a way to enhance the signal and increase its contribution in the far field.

Our experimental data are recorded from a single air gun, whereas in practice, big arrays and clusters are used for exploration. Therefore, an obvious solution is to tune air-gun arrays in the way that they create one big bubble (Hopperstad et al., 2012). The main advantage of these hyperclusters is that the bubble time period, and at the same time the low-frequency output, is increased. However, enhancements of even lower frequencies could be due to the rising of a big bubble. As a thought experiment, we assume an air-gun cluster with a circular shape (Figure 12), which could possibly create one big bubble. We compute new near-field amplitudes using our modeling for a rising sphere. We take the same density for the bubble as for the single air-gun bubble, but we increase the radius for the bubble created by the proposed array design, which is towed at 7.5 m depth. This array configuration could, in theory, be expanded to create even bigger bubbles. In practice, clusters are limited to the strength of mechanical structures and the supply of high-pressure air into one small location. This simple example should only illustrate which bubble sizes are roughly required to create applicable signals. Further investigation needs to be done on the separation between single guns, whether a frequency-locked array or an array with coalesced bubbles is optimal for the enhancement of this source mechanism (Laws et al., 1990). For bigger air bubbles, the source depth is also an important factor that needs to be taken into account.

Results for the achieved near-field amplitude for the low-frequency signal at 2 Hz could be enhanced as seen in Table 3 according to our thought experiment. The first four amplitudes up to a radius of 1 m are measured from the experimental data, where different radii result from the difference in source depth. The amplitudes for bigger radii are modeled assuming a rising sphere. If we were able to create a big bubble with $R = 15$ m, near-field amplitudes of the low frequencies would be increased by a factor of approximately 450 compared with a single air gun.

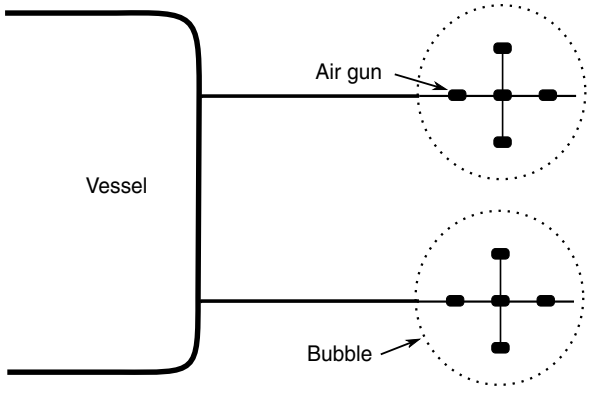

Figure 12. Possible array design for creating one big air bubble to enhance the proposed low-frequency signal. A bubble with $R \approx 3$ m could be expected for these number of air guns.

For field applications, we have to take the attenuation, geometric spreading, reflection coefficient, and especially the source-ghost effect into account (equation 19). Therefore, we compute the far-field amplitudes for the low-frequency signal after it has traveled through the same 3D medium as used earlier. Again, we assume two different velocities v_m and Q-values (Table 4). We also assume that the source is fired at three different depths z_s to demonstrate the impact of the ghost. We use a main frequency of 2 Hz, but it should be noted that this frequency will slightly change according to the source depth.

Two main features should be noted from the results in Table 4. First, the well-known effect of increased amplitudes in low frequencies with increasing source depth can be seen, assuming that the bubble size is constant. Second, the signal strength will be above the noise level for calm weather conditions, if the bubble radius exceeds 12 m. The amplitudes of the low-frequency signal could be higher if we are interested in diving waves because we can neglect the reflection coefficient. Changing the array design could also have negative

Table 3. Near-field amplitude of the signal from the rising bubble for source depth of $z_s = 7.5$ m. Measured single air-gun amplitude for $R \leq 1$ m and computed amplitude for bigger bubble radii $R > 1$ m using the proposed model.

Bubble radius R (m)	Amplitude (bar-m)
0.66	0.0030
0.75	0.0038
0.86	0.0049
1	0.0065
3	0.0520
6	0.2090
9	0.6180
12	1.5120
15	3.1830

Table 4. Computed far-field amplitudes (in bar) for the low-frequency signal from a rising air-gun bubble after traveling through a 3 km thick 3D medium with velocity v_m and quality factor Q. The amplitude is given for different source depths z_s and radii R of the bubble.

z_s (m)	$R = 6$ m	$R = 9$ m	$R = 12$ m	$R = 15$ m
	Case 1: $v_m = 3000$ (m/s), $Q = 150$			
7.5	8.05e-7	2.38e-6	5.82e-6	12.3e-6
10	1.07e-6	3.17e-6	7.76e-6	16.3e-6
15	1.61e-6	4.75e-6	11.6e-6	24.5e-6
	Case 2: $v_m = 4000$ (m/s), $Q = 300$			
7.5	8.48e-7	2.51e-6	6.13e-6	13.0e-6
10	1.13e-6	3.34e-6	8.17e-6	17.2e-6
15	1.69e-6	5.00e-6	12.2e-6	25.8e-6

impacts on the overall signal output, which was not investigated here. However, we demonstrated that there could be contributions from this source mechanism to the low-frequency end of the spectrum.

The maximum size of an air-gun bubble that is achievable in field applications is mainly an engineering issue and is not addressed in our investigations. Another approach to make the signal from the rising air-gun bubble applicable is to reduce the low-frequency noise on the recorded data. A better signal-to-noise ratio at these frequencies might be achieved by the use of 4C ocean-bottom recordings instead of streamer data (Landrø et al., 2014; Halliday et al., 2015).

CONCLUSION

The proposed mechanism that a moderate part of low frequencies could be created by the rising air-gun bubble could be confirmed from tank and field experiments, which are supported by a simple model. Further contributions could be due to the spike shape of the main impulse. The signal from the rising air-gun bubble shows increasing length and decreasing amplitude with increasing source depth, whereas it is clearer for shallow source depths, where less dissolution of the bubble on its rising path is expected. These features agree with the theory and model. The contribution from the rising bubble signal to the frequency spectrum of a single air-gun source in the far field is insignificant. However, there could be contributions from this mechanism if huge air-gun clusters are used and tuned as suggested here. This might exploit the mechanism to make it feasible for exploration purposes, especially for investigations of deep targets and crustal studies. The estimations are made on a simple model, and therefore further investigation is needed on whether this mechanism can contribute significantly within field applications. This involves more complex modeling with different array designs and studies of field data.

ACKNOWLEDGMENTS

We acknowledge the European Union's Horizon 2020 research and innovation program under the Marie Skłodowska-Curie grant agreement no. 641943 for the funding of D. Wehner's Ph.D. project within WAVES. We thank Statoil ASA for contributing the air-gun recordings, where Å. S. Pedersen and M. Thomson have designed and conducted the field work. We acknowledge the technical team at IPT for their support to the experimental setup. D. Wehner thanks K. E. Haavik for fruitful discussions. M. Landrø acknowledges financial support from the Norwegian Research Council. The editor and anonymous reviewers are acknowledged for their constructive comments.

REFERENCES

Abma, R., and A. Ross, 2013, Popcorn shooting: Sparse inversion and the distribution of airgun array energy over time: 83rd Annual International Meeting, SEG, Expanded Abstracts, 31–35.

Achenbach, E., 1972, Experiments on the flow past spheres at very high Reynolds numbers: Journal of Fluid Mechanics, **54**, 565–575, doi: 10.1017/S0022112072000874.

Cambois, G., A. Long, G. Parkes, T. Lundsten, A. Mattsson, and E. Fromyr, 2009, Multi-level airgun array: A simple and effective way to enhance the low frequency content of marine seismic data: 79th Annual International Meeting, SEG, Expanded Abstracts, 152–156.

Carlson, D., A. Long, W. Soellner, H. Tabti, R. Tenghamn, and N. Lunde, 2007, Increased resolution and penetration from a towed dual-sensor streamer: First Break, **25**, 71–77.

Coste, E., D. Gerez, H. Groenaas, J.-F. Hopperstad, O. P. Larsen, R. Laws, J. Norton, M. Padula, and M. Wolfstirn, 2014, Attenuated high-frequency emission from a new design of air-gun: 84th Annual International Meeting, SEG, Expanded Abstracts, 132–137.

Dellinger, J., A. Ross, D. Meaux, A. Brenders, G. Gesoff, J. T. Etgen, and J. Naranjo, 2016, Wolfspar, an FWI-friendly ultra-low-frequency marine seismic source: 86th Annual International Meeting, SEG, Expanded Abstracts, 4891–4895.

Dhelie, P. E., J. E. Lie, V. Danielsen, A. K. Evensen, and A. Myklebostad, 2014, Broadband seismic: A novel way to increase notch diversity: 84th Annual International Meeting, SEG, Expanded Abstracts, 148–152.

Dragoset, B., N. Hargreaves, and K. Larner, 1987, Air-gun source instabilities: Geophysics, **52**, 1229–1251, doi: 10.1190/1.1442385.

Gilmore, F. R., 1952, The growth or collapse of a spherical bubble in a viscous compressible liquid: Report, Hydrodynamics Laboratory, California Institute of Technology.

Haavik, K. E., and M. Landrø, 2015, Variable source depth acquisition for improved marine broadband seismic data: Geophysics, **80**, no. 3, A69–A73, doi: 10.1190/geo2014-0437.1.

Halliday, D., R. Laws, and M. Garden, 2015, Signal and noise in a shallow-water ocean-bottom cable survey: 85th Annual International Meeting, SEG, Expanded Abstracts, 120–124.

Halliday, D., R. Resnick, and W. Jearl, 2003, Fundamentals of physics: Wiley.

Hicks, E., H. Hoeber, G. Poole, and B. King, 2014, An efficient 4D processing flow for variable-depth streamer data: The Leading Edge, **33**, 172–180, doi: 10.1190/tle33020172.1.

Hopperstad, J.-F., R. Laws, and E. Kragh, 2012, Hypercluster of airguns: More low frequencies for the same quantity of air: 74th Annual International Conference and Exhibition, EAGE, Extended Abstracts, Z011.

Ikelle, L. T., and L. Amundsen, 2005, Introduction to petroleum seismology: SEG.

Landrø, M., and L. Amundsen, 2014a, Is it optimal to tow air guns shallow to enhance low frequencies?: Geophysics, **79**, no. 3, A13–A18, doi: 10.1190/geo2013-0348.1.

Landrø, M., and L. Amundsen, 2014b, Maximizing the ultra-low frequency output from air guns: 76th Annual International Conference and Exhibition, EAGE, Extended Abstracts, TuELI209.

Landrø, M., K. E. Haavik, and L. Amundsen, 2014, Using geophone components to obtain ultralow frequency seismic signals at long offsets: 84th Annual International Meeting, SEG, Expanded Abstracts, 233–237.

Landrø, M., R. Haugen, A. Sodal, E. Nielsen, and S. Vaage, 1989, Study of marine seismic noise recorded by M/V Bernier July/August 1988: SERES Report no. T.29.02/89.

Laws, R., L. Hatton, and M. Haartsen, 1990, Computer modeling of clustered airguns: First Break, **8**, 331–338, doi: 10.3997/1365-2397.1990017.

LeVeque, R. J., 2007, Finite difference methods for ordinary and partial differential equations: SIAM.

Mavko, G., T. Mukerji, and J. Dvorkin, 1998, The rock physics handbook: Cambridge University Press.

Meier, M. A., R. E. Duren, K. T. Lewallen, J. Otero, S. Heiney, and T. Murray, 2015, A marine dipole source for low frequency seismic acquisition: 85th Annual International Meeting, SEG, Expanded Abstracts, 176–180.

Michelson, I., 1970, The science of fluids: Van Nostrand Reinhold Company.

Moldoveanu, N., 2000, Vertical source array in marine seismic exploration: 70th Annual International Meeting, SEG, Expanded Abstracts, 53–56.

Morrison, F. A., 2013, An introduction to fluid mechanics: Cambridge University Press.

Ozasa, H., H. Mikada, F. Sato, F. Murakami, J. Takekawa, and E. Asakawa, 2015, Development of hydraulic low frequency marine seismic vibrator: 19th International Symposium on Recent Advances in Exploration Geophysics (RAEG 2015), doi: 10.3997/2352-8265.20140185.

Pramik, B., M. L. Bell, A. Grier, and A. Lindsay, 2015, Field testing the aquavib: An alternate marine seismic source: 85th Annual International Meeting, SEG, Expanded Abstracts, 181–185.

Reynolds, O., 1883, An experimental investigation of the circumstances which determine whether the motion of water shall be direct or sinuous, and of the law of resistance in parallel channels: Report, Proceedings of the Royal Society of London.

Robertsson, J. O. A., S. Ronen, S. Singh, and R. van Borselen, 2013, Broadband seismology in oil and gas exploration and production — Introduction: Geophysics, **78**, no. 2, WA1–WA2, doi: 10.1190/geo2013-0313-SPSEIN.1.

Soubaras, R., and Y. Lafet, 2013, Variable-depth streamer acquisition: Broadband data for imaging and inversion: Geophysics, **78**, no. 2, WA27–WA39, doi: 10.1190/geo2012-0297.1.

ten Kroode, F., S. Bergler, C. Corsten, J. W. de Maag, F. Strijbos, and H. Tijhof, 2013, Broadband seismic data: The importance of low frequencies: Geophysics, **78**, no. 2, WA3–WA14, doi: 10.1190/geo2012-0294.1.

Wei, Z., M. A. Hall, and T. F. Phillips, 2012, Geophysical benefits from an improved seismic vibrator: Geophysical Prospecting, **60**, 466–479, doi: 10.1111/j.1365-2478.2011.01008.x.